



The global properties of nocturnal stable atmospheric boundary layers

Zhouxing Shen¹, Luoqin Liu^{1,†}, Xiyun Lu¹ and Richard J.A.M. Stevens²

¹Department of Modern Mechanics, University of Science and Technology of China, Hefei 230027, Anhui, PR China

²Physics of Fluids Group, Max Planck Center Twente for Complex Fluid Dynamics, J. M. Burgers Center for Fluid Dynamics, University of Twente, P.O. Box 217, 7500 AE Enschede, The Netherlands

(Received 9 April 2024; revised 24 September 2024; accepted 6 October 2024)

Accurate prediction of the global properties of wall-bounded turbulence holds significant importance for both fundamental research and engineering applications. In atmospheric boundary layers, the relationship between friction drag and geostrophic wind is described by the geostrophic drag law (GDL). We use carefully designed large-eddy simulations to study nocturnal stable atmospheric boundary layers (NSBLs), which are characterized by a negative potential temperature flux at the surface and neutral stratification higher up. Our simulations explore a wider range of the Kazanski–Monin parameter, $\mu = L_f/L_s = [16.7, 193.3]$, with L_f the Ekman length scale and L_s the surface Obukhov length. We show collapse of the GDL coefficients onto single curves as functions of μ , thereby validating the GDL's applicability to NSBLs over a very wide μ range. We show that the boundary-layer height h scales with $\sqrt{L_f L_s}$, while both the streamwise and spanwise wind gradients scale with $u_*^2/(h^2 f)$, where u_* represents the friction velocity and f the Coriolis parameter. Leveraging these insights, we developed new analytical expressions for the GDL coefficients, significantly enhancing our understanding of the GDL for turbulent boundary layers. These formulations facilitate the analytical prediction of the geostrophic drag coefficient and cross-isobaric angle.

Key words: atmospheric flows, turbulent boundary layers

1. Introduction

A fundamental challenge in wall-bounded turbulent flow is to accurately predict global properties such as friction drag. This insight is also crucial for practical scenarios as friction drag can represent up to 90 % of the total drag in maritime navigation (Schultz *et al.* 2011) and 50 % in aviation (Spalart & McLean 2011). Additionally, accurately

† Email address for correspondence: luoqinliu@ustc.edu.cn

determining the friction velocity is required for a thorough analysis of the logarithmic law (Smits 2022). For rough surfaces, these predictions are more challenging as the impact of surface roughness is complicated (Chung *et al.* 2021). Thus, accurately characterizing the global properties of wall-bounded turbulence is an active research area and high-fidelity experiments and simulations are essential to advance our understanding of wall turbulence (Marusic & Monty 2019). For fully developed channel or pipe flows the friction velocity can be conveniently calculated using the pressure gradient. However, predicting this parameter for atmospheric boundary layers (ABLs) is more challenging and requires insight into the mean velocity gradient at the wall (Ricco & Skote 2022).

In contrast to canonical turbulent boundary layers, which are dominated by shear forces (Townsend 1976), the ABL is additionally influenced by Coriolis forces and thermal stratification (Stull 1988). Meanwhile, the Reynolds number of ABLs can be two orders of magnitude larger than what is possible in the laboratory (Smits, McKeon & Marusic 2011). Consequently, the prediction of the ABL turbulence is very challenging. In ABLs the geostrophic drag coefficient and the cross-isobaric angle can be estimated by the well-known geostrophic drag law (GDL), which was first proposed for neutral ABLs (Rossby & Montgomery 1935; Blackadar & Tennekes 1968; Tennekes & Lumley 1972; Tennekes 1973) and later extended to include the thermal stratification (Zilitinkevich 1969, 1975; Zilitinkevich & Esau 2002), unsteadiness (Zilitinkevich & Deardorff 1974; Arya 1975) and baroclinicity effects (Arya & Wyngaard 1975; Arya 1978; Hess 2004). For convective ABLs, the updrafts tend to transit from open cells to longitudinal rolls when the surface potential temperature flux decreases and the mean wind shear increases (Salesky, Chamecki & Bou-Zeid 2017). Recently, Tong & Ding (2020) derived a novel friction law for the convective ABLs in the roll-dominated regime, demonstrating that the friction velocity correlates with the mean wind speed in the mixed layer rather than with the geostrophic wind in the free atmosphere. This finding has been numerically confirmed by Liu, Gadde & Stevens (2023). For conventionally neutral ABLs, Liu, Gadde & Stevens (2021*a*) and Liu, Lu & Stevens (2024) have updated GDL parameterizations by performing high-fidelity simulations.

When atmospheric flows are stably stratified near the surface and develop against a neutrally stratified flow above, the ABL is considered to be nocturnally stable (Zilitinkevich & Esau 2005). Nocturnal stable atmospheric boundary layers (NSBLs) have negative potential temperature fluxes at the surface and neutral stratification aloft. They prevail at nocturnal conditions but can also survive for several hours after sunrise over continental lands and persist continuously for days in polar regions (Mahrt 2014). Their global properties (e.g. the boundary-layer height, the geostrophic drag coefficient and the cross-isobaric angle) are crucial for the heat, mass and momentum exchange between the surface and the free atmosphere. Understanding these boundary layers is of great fundamental interest and very relevant for meteorological applications (LeMone *et al.* 2019). However, so far, the understanding of NSBLs remains limited, and in this work, we therefore focus on a detailed characterization of their global properties using simulations and theoretical analysis.

In this study, we consider the NSBLs under quasi-steady, barotropic and horizontally homogeneous conditions. For simplicity, we focus on the Northern Hemisphere with latitude $\phi > 0$ so that the Coriolis parameter $f = 2\Omega \sin \phi > 0$, where $\Omega = 0.729 \times 10^{-4} \text{ rad s}^{-1}$ is the rotation rate of the Earth. Then, it follows from dimensional analysis that the dynamics in NSBLs is governed by only two independent dimensionless parameters, e.g. the Rossby number $Ro = u_*/(fz_0)$ (Rossby & Montgomery 1935) and the Kazanski–Monin parameter $\mu = L_f/L_s$ (Kazanski & Monin 1961), where u_* is the friction velocity, z_0 is the roughness height, $L_f = u_*/f$ is the Ekman length scale (Ekman 1905)

and $L_s = -u_*^3/(\beta q_s)$ is the surface Obukhov length (Obukhov 1946) with β denoting the buoyancy parameter and q_s the surface potential temperature flux. The Rossby number characterizes the relative importance of the Coriolis force and friction drag and the Kazanski–Monin parameter μ represents the strength of thermal stratification near the surface, which varies within the interval $-10^3 < \mu < 10^3$ in the atmosphere. For $|\mu| \ll 10$ the ABL is traditionally considered neutral (Zilitinkevich & Esau 2002); while for $\mu = O(10^3)$, the ABL turbulence is intermittent and may no longer fully satisfy the usual conditions for the definition of turbulence (Mahrt 2014). Therefore, in this study we only consider the NSBLs with $\mu = O(10) \sim O(10^2)$.

We consider the coordinate system that is oriented such that the streamwise direction is parallel to the wind direction at the surface, and the spanwise direction is orthogonal to the streamwise and vertical directions (see figure 1). Then, the GDL for the quasi-steady, barotropic and horizontally homogeneous NSBLs can be written as (e.g. Zilitinkevich & Esau 2005)

$$A = \ln Ro - \frac{\kappa U_g}{u_*}, \quad B = -\frac{\kappa V_g}{u_*}, \quad (1.1a,b)$$

where $\kappa = 0.4$ is the von Kármán constant, (U_g, V_g) are the streamwise and spanwise components of the geostrophic wind, which are assumed to be independent of height z , and A and B are the GDL coefficients. Blackadar & Tennekes (1968) proved using similarity and asymptotic analysis that for neutral ABLs the A and B parameters are independent of the Rossby number, Ro . This analysis also gives that, for NSBLs, A and B only depend on the Kazanski–Monin parameter μ , see also Zilitinkevich (1975). The geostrophic drag coefficient $u_*/(U_g^2 + V_g^2)^{1/2}$ and the cross-isobaric angle $\alpha_0 = \arctan(|V_g/U_g|)$ can be determined from (1.1a,b). Therefore, the A and B coefficients are critical in estimating available wind resources at higher elevations by extrapolating wind profiles beyond the surface layer (Gryning *et al.* 2007; Kelly & Gryning 2010). Note that similar drag relations also exist for various wall-bounded turbulent flows, such as turbulent boundary-layer flow, channel flow and pipe flow (Pope 2000; Marusic *et al.* 2013). Due to the absence of Coriolis forces, the corresponding friction laws relate only to (1.1a) and are traditionally expressed through the Reynolds number.

The GDL coefficients A and B can be parameterized through two main approaches. One is by parameterizing the eddy viscosity profile (Rossby & Montgomery 1935; Ellison 1955; Krishna 1980; Kadantsev, Mortikov & Zilitinkevich 2021), and the other is by parameterizing the mean velocity profiles (Zilitinkevich 1989b,a; Zilitinkevich *et al.* 1998; Zilitinkevich & Esau 2005; Narasimhan, Gayme & Meneveau 2024). Then, an asymptotic matching of the inner layer velocity profile with the outer layer is used to determine the final expressions of the GDL coefficients A and B . For example, Kadantsev *et al.* (2021) derived analytical expressions for A and B by assuming that the eddy viscosity satisfies a linear profile in the surface layer and a constant profile in the Ekman layer. However, this eddy viscosity approximation is inconsistent with that proposed by Basu & Holtslag (2023), who derived the eddy viscosity directly from the Ekman equations by assuming a power law of the total turbulent shear stress.

Based on the assumed velocity and its gradient profiles, Zilitinkevich & Esau (2005) proposed the following expressions of the GDL coefficients A and B for quasi-steady and barotropic NSBLs:

$$A = -am_A + \ln(a_0 + m_A) - \ln\left(\frac{h}{L_f}\right), \quad B = \frac{h}{L_f}(b_0 + bm_B^2). \quad (1.2a,b)$$

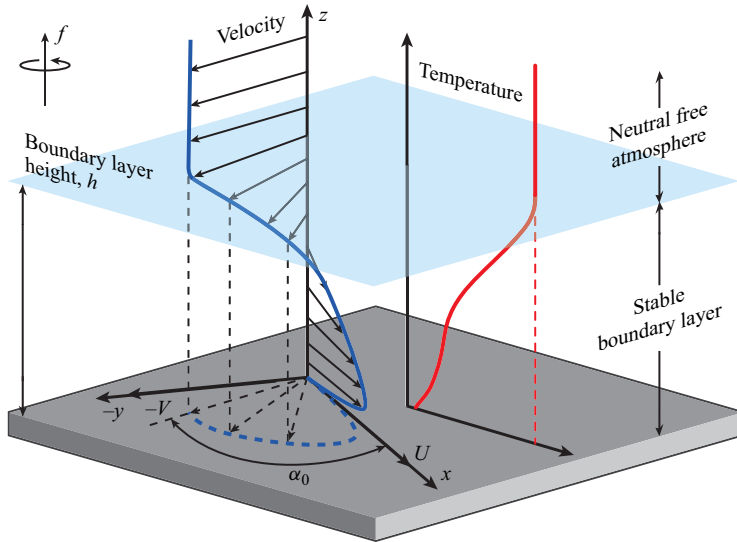


Figure 1. Schematic representation of NSBLs (not to scale). It shows the velocity and potential temperature profiles as a function of height, the definition of boundary-layer depth and the typical Ekman spiral in the boundary layer. Here, f is the Coriolis parameter, h is the boundary-layer height, α_0 is the angle between the surface stress and the geostrophic wind and (U, V) are the velocity components along the (x, y) axes, respectively. The x axis is parallel to the wind on the surface, the z axis points upwards and (x, y, z) forms a right-handed coordinate system.

Here, (a, a_0, b, b_0) are empirical constants, h is the boundary-layer height and (m_A, m_B) are the composite stratification parameters

$$m_A^2 = \left(\frac{h}{L_s}\right)^2 + \left(\frac{c_{fa}h}{L_f}\right)^2, \quad m_B^2 = \left(\frac{h}{L_s}\right)^2 + \left(\frac{c_{fb}h}{L_f}\right)^2, \quad (1.3a,b)$$

where (c_{fa}, c_{fb}) are empirical constants. To obtain the values of A and B analytically, the boundary-layer height h of quasi-steady and barotropic NSBLs is parameterized as (Zilitinkevich, Esau & Baklanov 2007)

$$\left(\frac{L_f}{h}\right)^2 = \frac{1}{c_r^2} + \frac{\mu}{c_s^2}, \quad (1.4)$$

where (c_r, c_s) are empirical constants.

Given the critical importance of GDL parameterization for both theoretical research and practical applications, it is essential to investigate the GDL expressions of A and B for NSBLs proposed by Zilitinkevich & Esau (2005). In their analysis of the GDL, Zilitinkevich & Esau (2005) divided the surface layer into a logarithmic layer and a z -less stratification layer. Subsequently, they constructed the streamwise and spanwise velocities using the eddy viscosity approach and the assumption that the streamwise and spanwise velocity gradients above the surface layer scale as u_*/L_s and h^2f/L_s^2 , respectively. The term ‘ z -less stratification’ was first used by Wyngaard & Coté (1972), which indicates that the height z is no longer a primary scaling variable for very stable ABLs. However, the validity of z -less stratification is still an open question that requires further clarification (Grachev *et al.* 2013). For example, it is assumed to happen under very stable stratification (Mahrt 2014), but has also been reported in weakly stable conditions (Stiperski & Calaf

2018). Note that the existence of a z -less stratification layer is not a prerequisite for the validity of the GDL. In other words, the division of the surface layer into a logarithmic layer and a z -less stratification layer is not necessary for deriving the expressions of A and B . In addition, our analysis will show that there is no z -less stratification layer in the weakly stable conditions considered in this study. Therefore, removing the concept of z -less stratification from the analysis of the GDL may lead to a derivation that helps reveal the essential assumptions and underlying physics of the GDL.

Due to the significant challenges in atmospheric measurements (Fernando & Weil 2010), high-fidelity data from field experiments are very limited. With the rapid advancement of computational methods, obtaining simulation results for wall-bounded turbulent flows has now become a feasible method to produce high-fidelity data for model development. As the Reynolds number in ABLs is very high, large-eddy simulation (LES) is a widely accepted technique to model these flows (Kim & Leonard 2024). However, extensive datasets, covering a wide parameter range for μ and Ro for NSBLs are very rare. Zilitinkevich & Esau (2005) obtained their database using LES on a 64^3 mesh and used the dynamic mixed subgrid-scale (SGS) model (Vreman, Geurts & Kuerten 1994). Despite significant scatter, Kadantsev *et al.* (2021) also used this database to investigate their newly derived GDL. The grid convergence of stable ABL simulations has been investigated and was found to depend on various factors such as the wall modelling (Maronga, Knigge & Raasch 2020), the roughness length (Couvreur *et al.* 2020), the SGS model (Dai *et al.* 2021) and numerical schemes (Maronga & Li 2022). Although this issue remains partially unresolved, it is widely accepted that the lowest grid level should exceed the lower limit of the inertial sublayer (Basu & Lacser 2017). Furthermore, Maronga & Li (2022) demonstrated that simulation duration is critically important to minimize the influence of inertial oscillations on the results (Van de Wiel *et al.* 2010). Taking these lessons into account, we have performed a unique set of simulations covering a wide range of Ro and μ , that facilitates a robust evaluation of GDL parameters without scatter in global flow properties.

The organization of the paper is as follows. In § 2, we discuss the simulation design. In § 3, we show that the boundary-layer height scales as $\sqrt{L_f L_s}$ and the wind gradients scale as $u_*^2/(h^2 f)$. With these physical insights, we derive the GDL coefficients A and B in § 4, which avoids the concept of the z -less stratification layer. In § 5, we show that A and B obtained from LES collapse to a single curve as function of μ , which is well captured by the presented GDL parameterization for NSBLs given by (1.1a,b). We conclude with a summary of the main findings in § 6.

2. Large-eddy simulation framework

2.1. Governing equations

We use LES to simulate the NSBL flow over an infinite flat surface with homogeneous roughness. We integrate the spatially filtered continuity equation, momentum equation and potential temperature equation (Albertson 1996; Albertson & Parlange 1999; Liu *et al.* 2021a; Liu, Gadde & Stevens 2021b)

$$\nabla \cdot \tilde{\mathbf{u}} = 0, \quad (2.1)$$

$$\partial_t \tilde{\mathbf{u}} + \tilde{\boldsymbol{\omega}} \times \tilde{\mathbf{u}} = f \mathbf{e}_z \times (\mathbf{G} - \tilde{\mathbf{u}}) + \beta(\tilde{\theta} - \langle \tilde{\theta} \rangle) \mathbf{e}_z - \nabla \tilde{p} - \nabla \cdot \boldsymbol{\tau}, \quad (2.2)$$

$$\partial_t \tilde{\theta} + \tilde{\mathbf{u}} \cdot \nabla \tilde{\theta} = -\nabla \cdot \mathbf{q}, \quad (2.3)$$

where the tilde denotes spatial filtering, $\langle \cdot \rangle$ represents horizontal averaging, $\tilde{\mathbf{u}}$ is the velocity, $\tilde{\boldsymbol{\omega}} = \nabla \times \tilde{\mathbf{u}}$ is the vorticity, \tilde{p} is the modified pressure departure from equilibrium,

$\tilde{\theta}$ is the potential temperature, β is the buoyancy parameter, $\mathbf{G} = (U_g, V_g, 0)$ is the geostrophic wind velocity, $\boldsymbol{\tau}$ denotes the deviatoric part of the SGS shear stress and \mathbf{q} represents the SGS potential temperature flux. Molecular viscosity is neglected as the Reynolds number of atmospheric flows is very high.

For closure of (2.1)–(2.3), we parameterize the SGS shear stress and potential temperature flux as

$$\boldsymbol{\tau} = -2\nu_t \tilde{\mathbf{S}}, \quad \mathbf{q} = -\nu_\theta \nabla \tilde{\theta}, \quad \tilde{\mathbf{S}} \equiv \frac{1}{2} [\nabla \tilde{\mathbf{u}} + (\nabla \tilde{\mathbf{u}})^T], \quad (2.4a-c)$$

where ν_t and ν_θ are the eddy viscosity and eddy diffusivity, respectively, and $\tilde{\mathbf{S}}$ is the resolved strain-rate tensor with the superscript T denoting a matrix transpose. We use the anisotropic minimum dissipation (AMD) model (Abkar & Moin 2017), which has been extensively validated (Gadde, Stieren & Stevens 2021), to perform the simulations. In the AMD model, the eddy viscosity and eddy diffusivity are determined so that the energy of the sub-filter scales of the LES solution does not increase with time.

2.2. Numerical method

Our code is an updated version of the one used by Albertson & Parlange (1999). The grid points are uniformly distributed, and the computational planes for horizontal and vertical velocities are staggered in the vertical direction. The first vertical velocity grid plane is located at the ground, and the first streamwise and spanwise velocities and potential temperature grid planes are located at half a grid distance away from the ground (Albertson 1996). In the vertical direction, we use a second-order finite difference method, while we use a pseudo-spectral discretization with periodic boundary conditions in the horizontal directions. Time integration is performed using the second-order Adams–Bashforth method. The projection method is used to ensure the divergence-free condition of the velocity field.

At the top boundary the vertical velocity, the SGS shear stress and the SGS potential temperature flux are enforced to zero, while the potential temperature is imposed by a constant value. In the top 25 % of the domain a Rayleigh damping layer with the damping frequency 0.001 s^{-1} determined by trial and error is applied every time step to reduce the effects of gravity waves (Klemp & Lilly 1978; Liu & Stevens 2021). At the bottom boundary, we employ a wall model based on the Monin–Obukhov similarity theory (MOST) for both the velocity field and the potential temperature field (Monin & Obukhov 1954; Moeng 1984; Stoll & Porté-Agel 2008; Liu & Stevens 2021)

$$u_* = \frac{\kappa (\overline{u^2} + \overline{v^2})^{1/2}}{\ln(z/z_0) - \psi_m}, \quad q_s = \frac{\kappa u_* (\theta_s - \tilde{\theta})}{\ln(z/z_0) - \psi_h}, \quad (2.5a,b)$$

where the overline denotes filtering at a scale of 2Δ with $\Delta = (\Delta x \Delta y \Delta z)^{1/3}$ the filter scale of (2.1)–(2.3) and Δx , Δy , Δz the grid spacings in the streamwise, spanwise and vertical directions, respectively, and where θ_s is the potential temperature at the surface, and ψ_m and ψ_h are, respectively, the stability corrections for the momentum and potential temperature fluxes, which for NSBLs can be parameterized as (Businger *et al.* 1971; Stull 1988; Huang & Bou-Zeid 2013; Sullivan *et al.* 2016; Abkar & Moin 2017)

$$\psi_m = -4.8\kappa z/L_s, \quad \psi_h = -7.8\kappa z/L_s, \quad z/L_s \geq 0. \quad (2.6a-c)$$

Note that the definition of L_s in this study is the same as Zilitinkevich & Esau (2005) but different from Liu & Stevens (2021), and thus the constant κ appears in (2.6a–c).

In addition, we note that the MOST, which is the basis of the wall model (2.5a,b), has been confirmed by various direct numerical simulations (e.g. Shah & Bou-Zeid 2014) and field experiments (e.g. Businger *et al.* 1971). Since the MOST is generally valid in the surface layer of the ABLs in weakly stable regime (Grachev *et al.* 2005; Katul, Konings & Porporato 2011; Stoll *et al.* 2020), the wall model based on the MOST is used in this study.

2.3. Computational set-up

To obtain simulation results independent of the computational domain, the domain size in each direction has to be several times the size of the largest eddies or the boundary-layer height (Couvreur *et al.* 2020). The selected computational domain size is $800\text{ m} \times 800\text{ m} \times 800\text{ m}$ in the streamwise, spanwise and vertical directions, respectively. As shown in table 1, the deepest boundary-layer height is approximately 266 m, which is less than one third of the computational domain size. Since the MOST-based wall model is employed, the lowest grid level z_1 should be above the lower limit of the inertial sublayer z_* (Basu & Lacser 2017). The parameter z_* can be related to the roughness length z_0 , and their ratio depends on the atmospheric stability. In particular, for stably stratified conditions, the ratio z_*/z_0 for the wind profile was found to be significantly lower, approximately in the range of $11 \sim 55$ (Garratt 1983; Basu & Lacser 2017). Meanwhile, z_1 should be below the upper limit of the inertial sublayer, i.e. the Ozmidov length $L_O = (\varepsilon/N^3)^{1/2}$, where ε is the mean viscous dissipation and N is the Brunt–Väisälä frequency (Dougherty 1961; Ozmidov 1965; Huang & Bou-Zeid 2013; Sullivan *et al.* 2016). We select the grid resolution as $192 \times 192 \times 201$ such that the grid is nearly isotropic (Gadde *et al.* 2021), and, more importantly, $z_1/z_0 \geq 20$ since $z_0 \leq 0.1\text{ m}$ (see table 1). At the same time, this grid also satisfies the grid resolution requirement $z_1/L_O < 1$ (see figure 3 below).

The simulations are initialized with a constant potential temperature $\theta = 265\text{ K}$ and a constant geostrophic wind speed $G = 8 \sim 12\text{ m s}^{-1}$. Turbulence is triggered by adding random perturbations. A random noise term with a magnitude of 3% of the geostrophic wind speed is added to velocities below 50 m, and for the potential temperature a noise term with an amplitude of 0.1 K is added. The reference temperature is set to $\theta_0 = 263.5\text{ K}$. The latitude ϕ varies between 30° and 73° , and the surface cooling rate is set to $C_r = 0.05 \sim 0.35\text{ K h}^{-1}$. The roughness length is $z_0 = 0.001 \sim 0.1\text{ m}$. To remove the effects of slowly decaying inertial oscillations on the top of the domain (Van de Wiel *et al.* 2010; Maronga & Li 2022), the initial transient period lasts for 1.5 inertial time periods and the statistics are collected over the following one inertial period, i.e. $ft \in [3\pi, 5\pi]$ (see figure 2). This ensures the flow has reached its quasi-stationary state and the changes of u_* and α_0 are less than 5% of their mean values (see figure 2). We note that many time steps ($\sim O(10^7)$) are required to resolve the large range of relevant time scales in the problem, spanning from small-scale turbulence to large-scale inertial oscillations. A summary of these simulations is given in table 1, where the cases are arranged such that the value of ϕ increases monotonically from upper to lower rows.

We remark that the simulation input parameters of case 20 are the same as the standard Global Energy and Water Cycle Experiment Atmospheric Boundary Layer Study case (Beare *et al.* 2006; Liu & Stevens 2021), with the only exception being that the free-atmosphere lapse rate has been set as zero to ensure the flow belongs to the NSBL regime (Maronga *et al.* 2020). Besides, we remark that the simulations of Zilitinkevich & Esau (2005) that will be used for comparison were performed for $ft = 2.1\pi$, with time averaging over the period $ft \in [1.3\pi, 2.1\pi]$. As shown in figure 2, a time averaging should

| Case no. | ϕ (deg.) | C_r (K h^{-1}) | z_0 (m) | G (m s^{-1}) | α_0 (deg.) | u_* (m s^{-1}) | $h_{0,05}$ (m) | A | B | μ | Ro |
|----------|------------------|--------------------------------|--------------|------------------------------|----------------------|--------------------------------|-------------------|-------|------|-------|--------------------|
| 1 | 30 | 0.26 | 0.1 | 8 | 43.5 | 0.161 | 99.2 | -4.38 | 13.7 | 172.7 | 2.21×10^4 |
| 2 | 30 | 0.29 | 0.1 | 8 | 44.2 | 0.156 | 92.6 | -4.73 | 14.3 | 193.3 | 2.14×10^4 |
| 3 | 40 | 0.27 | 0.1 | 11 | 37.4 | 0.279 | 180 | -2.21 | 9.58 | 81.47 | 2.98×10^4 |
| 4 | 40 | 0.32 | 0.01 | 9 | 37.6 | 0.184 | 99.7 | -3.30 | 11.9 | 126.7 | 1.96×10^5 |
| 5 | 40 | 0.34 | 0.1 | 10 | 40.1 | 0.233 | 132 | -3.01 | 11.0 | 110.1 | 2.49×10^4 |
| 6 | 40 | 0.35 | 0.01 | 8 | 39.3 | 0.157 | 80.5 | -3.76 | 12.9 | 156.3 | 1.67×10^5 |
| 7 | 50 | 0.20 | 0.001 | 12 | 26.4 | 0.270 | 180 | -1.23 | 7.89 | 52.78 | 2.42×10^6 |
| 8 | 50 | 0.20 | 0.1 | 9 | 35.2 | 0.256 | 166 | -1.48 | 8.11 | 55.58 | 2.29×10^4 |
| 9 | 50 | 0.31 | 0.1 | 8 | 40.0 | 0.198 | 103 | -2.57 | 10.4 | 91.83 | 1.78×10^4 |
| 10 | 50 | 0.35 | 0.1 | 8 | 41.1 | 0.191 | 94.9 | -2.87 | 11.0 | 103.1 | 1.71×10^4 |
| 11 | 60 | 0.05 | 0.01 | 9 | 23.1 | 0.268 | 266 | -0.11 | 5.28 | 16.68 | 2.12×10^5 |
| 12 | 60 | 0.10 | 0.001 | 10 | 22.7 | 0.247 | 194 | -0.47 | 6.26 | 29.01 | 1.95×10^6 |
| 13 | 60 | 0.18 | 0.1 | 9 | 33.1 | 0.274 | 180 | -1.04 | 7.19 | 41.52 | 2.17×10^4 |
| 14 | 60 | 0.25 | 0.1 | 8 | 36.6 | 0.224 | 124 | -1.67 | 8.50 | 60.67 | 1.78×10^4 |
| 15 | 60 | 0.30 | 0.001 | 10 | 29.3 | 0.216 | 113 | -1.80 | 9.07 | 70.39 | 1.71×10^6 |
| 16 | 70 | 0.10 | 0.01 | 9 | 25.4 | 0.259 | 199 | -0.38 | 5.95 | 25.26 | 1.89×10^5 |
| 17 | 70 | 0.10 | 0.01 | 10 | 24.9 | 0.288 | 229 | -0.34 | 5.84 | 23.26 | 2.10×10^5 |
| 18 | 70 | 0.13 | 0.01 | 8 | 27.6 | 0.224 | 151 | -0.66 | 6.62 | 34.04 | 1.64×10^5 |
| 19 | 70 | 0.15 | 0.01 | 8 | 28.6 | 0.220 | 140 | -0.81 | 6.97 | 38.15 | 1.60×10^5 |
| 20 | 73 | 0.25 | 0.1 | 8 | 35.5 | 0.235 | 127 | -1.37 | 7.91 | 51.16 | 1.68×10^4 |

Table 1. Summary of simulations performed on the domain size $800 \text{ m} \times 800 \text{ m} \times 800 \text{ m}$ and $192 \times 192 \times 201$ grid points, where $h_{0,05}$ is defined at the height where the total shear stress reduces to 5% of its surface value and $\mu = L_f/L_s$ with the Obukhov length $L_s = -u_*^3/(\beta q_s)$.

The global properties of nocturnal stable ABLs

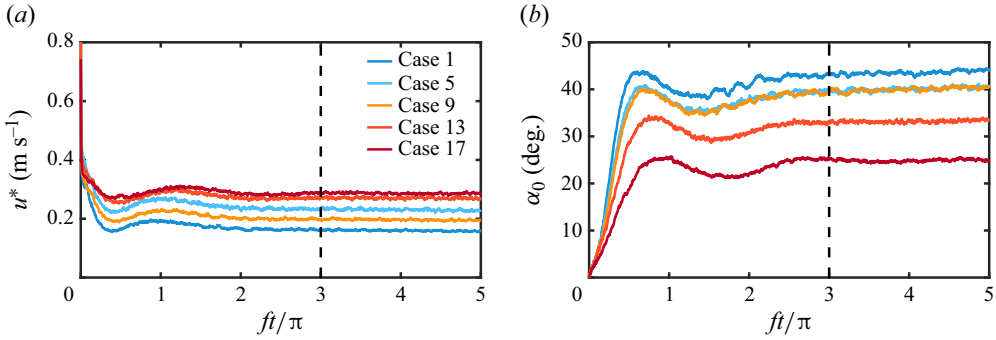


Figure 2. The time history of the domain-averaged (a) friction velocity u_* and (b) cross-isobaric angle α_0 . The solid lines are the simulation cases of table 1, and the dashed line denotes the beginning of the time-averaging window.

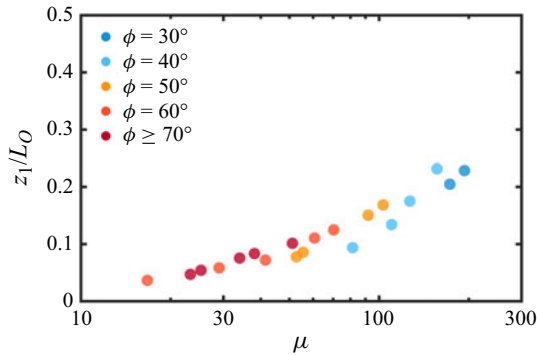


Figure 3. The ratio z_1/L_0 vs the Kazanski–Monin parameter μ . The simulation data are from table 1 and the Ozmidov length L_0 is calculated at $z = z_1$ (the lowest grid level).

start around $ft \approx 3\pi$ to ensure reliable determination of the friction velocity u_* and the cross-isobaric angle α_0 . This is the main reason for the large scatter of the simulation data of Zilitinkevich & Esau (2005). In contrast, the simulation data obtained from our LES with much longer simulation time show very limited scatter (see below).

It is well known that sufficient grid resolution is important in simulating stable ABLs with low turbulence levels (Huang & Bou-Zeid 2013; Maronga & Li 2022). Therefore, a quantitative investigation into the appropriateness of the chosen grid resolution is performed. Figure 3 shows that for all simulated cases the ratio $z_1/L_0 < 1$, which justifies the use of the MOST-based wall model. Similar to Sullivan *et al.* (2016), figure 3 shows that the Ozmidov length L_0 decreases as the cooling rate C_r increases. Thus, if a much larger cooling rate, e.g. $C_r = 2.5 \text{ K h}^{-1}$ (Huang & Bou-Zeid 2013), is considered, a higher grid resolution may be needed. However, for the cooling rate range $C_r = 0.05 \sim 0.35 \text{ K h}^{-1}$ considered here, the chosen grid resolution meets the required standards.

To further illustrate the effect of grid resolution on simulation results, figure 4 shows the mean vertical profiles of the wind speed, potential temperature, total shear stress and potential temperature flux for case 2 in table 1, which has the largest value of $\mu = 193.3$ and hence may have the strongest dependence on the grid resolution. The figure indicates that the magnitudes of the total shear stress and potential temperature flux in the boundary layer, as well as the boundary-layer height, decrease slightly as the grid resolution increases. This lack of strictly grid convergence in LES of the stable boundary

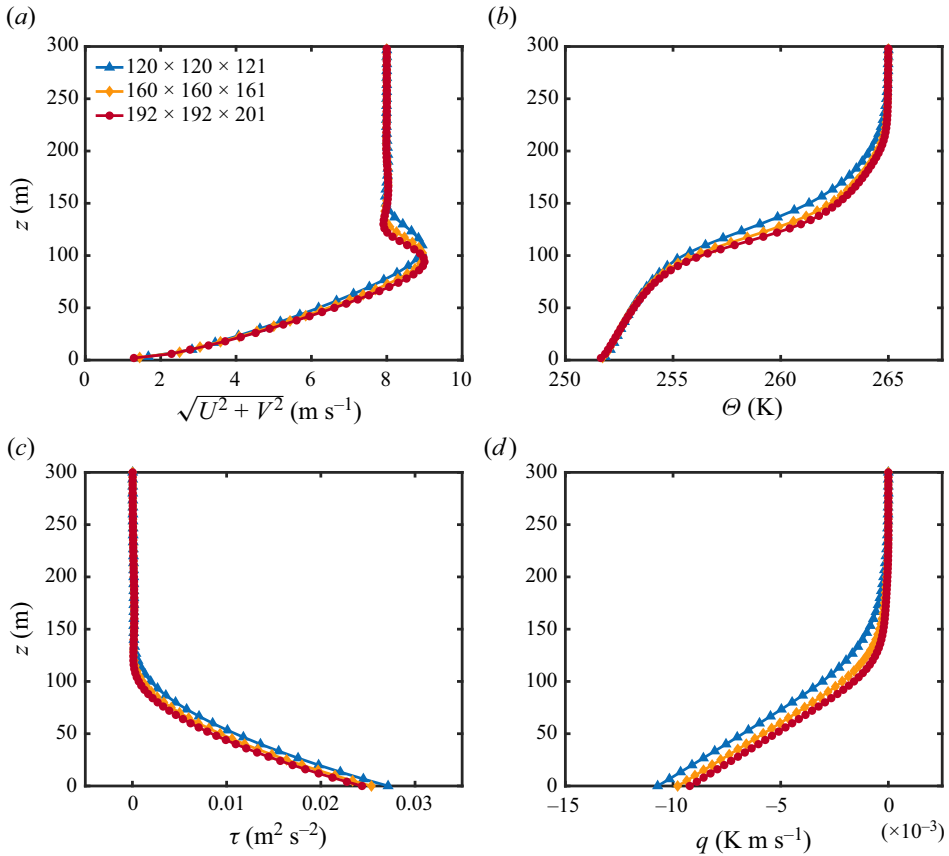


Figure 4. The grid dependence of the mean vertical profiles of the (a) wind speed $\sqrt{U^2 + V^2}$, (b) potential temperature θ , (c) total shear stress τ and (d) potential temperature flux q . The simulated case is case 2 with $\mu = 193.3$ in table 1.

layer is well known and remains partially unresolved (Maronga & Li 2022). Nevertheless, figure 4 shows that the mean vertical profiles with medium and dense grid resolutions do not change significantly. This finding confirms the appropriateness of the adopted grid resolution of $192 \times 192 \times 201$ in this study.

3. Boundary-layer height and wind gradient profiles

3.1. Boundary-layer height

In stable ABL flows the profile of the magnitude of total turbulent shear stress τ is often expressed as follows (Nieuwstadt 1984; Sorbjan 1986; Basu & Holtslag 2023):

$$\frac{\tau}{u_*^2} = \left(1 - \frac{z}{h}\right)^\alpha. \tag{3.1}$$

We remark that (3.1) was proposed under quasi-steady, barotropic and horizontally homogeneous conditions (Nieuwstadt 1984). Thus, it might not be valid for unsteady (Mahrt 2014; Momen & Bou-Zeid 2017), baroclinic (Arya & Wyngaard 1975; Floors, Peña & Gryning 2015; Momen *et al.* 2018) or surface heterogeneous (Schmid *et al.* 2019; Cooke, Jerolmack & Park 2024) flows. In addition, we remark that many different

The global properties of nocturnal stable ABLs

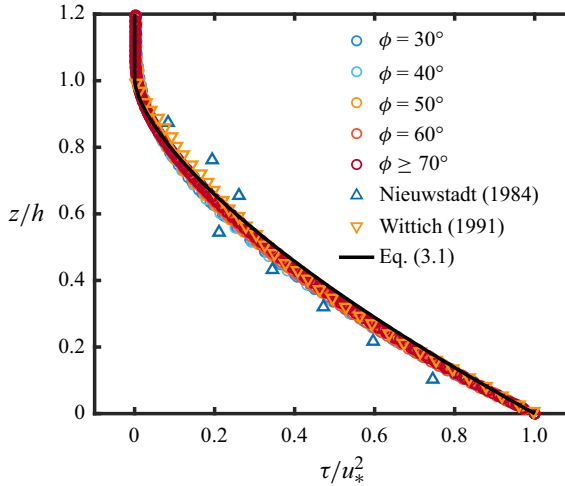


Figure 5. The profile of normalized total turbulent shear stress. Open circles: simulation data from [table 1](#); open triangles: field data of Nieuwstadt (1984); open inverted triangles: field data of Wittich (1991); solid line: prediction of (3.1) with $\alpha = 3/2$.

definitions of the stable ABL height h are available in literature, such as (a) the layer through which surface-based turbulence extends, (b) the top of the layer with downward potential temperature flux, (c) the height of the low-level jet and (d) the top of the potential temperature inversion layer (Vickers & Mahrt 2004).

In this study, we adopt definition (a). Specifically, the boundary-layer height h is defined as the height at which the total shear stress first vanishes. In particular, h is proportional to the height $h_{0.05}$, where the total shear stress reduces to 5% of its surface value (van Dop & Axelsen 2007; Liu *et al.* 2021b)

$$\frac{h_{0.05}}{h} = 1 - 0.05^{1/\alpha}. \quad (3.2)$$

By utilizing his local scaling hypothesis and the constant assumption of the flux Richardson number, Nieuwstadt (1984) determined analytically that the exponent $\alpha = 3/2$. Note that the value of α may not be a universal constant and other values of α have also been reported in the literature (Caughey, Wyngaard & Kaimal 1979; Yokoyama, Gamo & Yamamoto 1979; Lacser & Arya 1986; Sorbjan 1986; Lenschow *et al.* 1988; Byun 1991; Delage 1997).

Figure 5 shows the profile of normalized total turbulent shear stress in NSBLs. The open circles are the simulation data from [table 1](#), the open triangles are the field data taken from Nieuwstadt (1984), the open inverted triangles are the field data of Wittich (1991) and the solid line is the prediction of (3.1) with $\alpha = 3/2$. The good agreement of simulation data with field measurements validates our simulation results. Furthermore, our simulations indicate that the 3/2-law of total turbulent shear stress proposed by Nieuwstadt (1984) describes the data across the entire parameter range considered here.

For NSBLs with large values of μ , the parameterization of the boundary-layer height h given by (1.4) can be approximated as

$$\frac{h}{L_f} = \frac{c_s}{\sqrt{\mu}}, \quad (3.3)$$

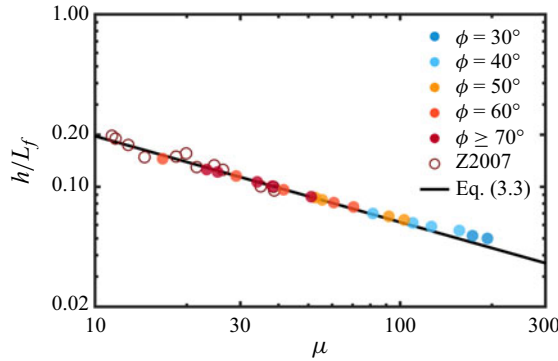


Figure 6. The dimensionless boundary-layer height h/L_f vs the Kazanski–Monin parameter μ . Filled circles: simulation data of table 1; open circles: simulation data of Zilitinkevich *et al.* (2007); solid line: prediction of (3.3) with $c_s = 0.62$ obtained by a least-squares fit.

where c_s is the Zilitinkevich constant (Derbyshire 1990), which depends on the definition of the boundary-layer height h . Equation (3.3) was originally proposed by Zilitinkevich (1972) based on boundary-layer scaling arguments and implies that the boundary-layer height h scales as $\sqrt{L_f L_s}$. Based on this definition, Zilitinkevich (1989*b*) summarized c_s from several studies and found it to vary between 0.55 and 1.58. This large variation affects the values of other empirical constants in the GDL formulation of Zilitinkevich & Esau (2005). As shown below, this is not the case for our formulation, where only the scaling of (3.3) matters while the value of c_s is irrelevant. This is also the case for the value of α since it can be absorbed into c_s , see (3.2) and (3.3). Recently, Basu & Holtslag (2023) derived two different eddy viscosity profile formulations, both leading to the boundary-layer height parameterization of Zilitinkevich (1972). The two derivations give $c_s = 0.922$ and $c_s = 0.658$, respectively, and they argued that the Zilitinkevich constant $c_s = 0.658$ seems to be a better option. More recently, Narasimhan *et al.* (2024) also reported $c_s = 0.78$ based on their LES data.

Figure 6 compares the dimensionless boundary-layer height h/L_f obtained from the present simulations of table 1 (filled circles), the simulation data of Zilitinkevich *et al.* (2007) (open circles) and the prediction of (3.3) with $c_s = 0.62$, which is determined using a least-squares fitting procedure based on the present LES database. All symbols collapse to a single curve, indicating that the dimensionless boundary-layer height h/L_f indeed only depends on the Kazanski–Monin parameter μ . The good agreement between the simulation data and theoretical prediction confirms the validity of the boundary-layer height parameterization of (3.3) over a much wider range of μ than Zilitinkevich *et al.* (2007) considered. Note that the simulation data of Zilitinkevich *et al.* (2007), which have a smaller range of μ than the present study, are very close to our theoretical model and simulation results.

3.2. Wind gradient profiles

Recall that we focus on the quasi-steady and barotropic NSBLs in weakly stable regime, whose dynamics is governed by the Ekman equations

$$\frac{d\tau_x}{dz} = -f(V - V_g), \quad \frac{d\tau_y}{dz} = f(U - U_g), \quad (3.4a,b)$$

The global properties of nocturnal stable ABLs

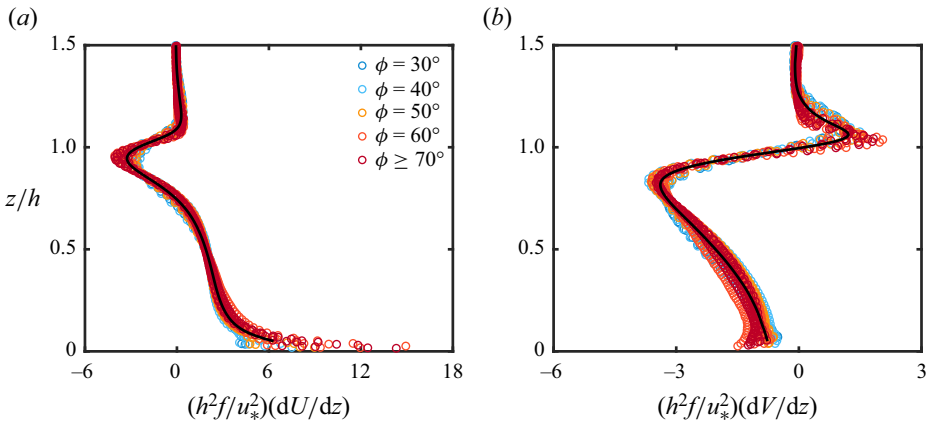


Figure 7. The vertical profiles of the normalized (a) streamwise and (b) spanwise velocity gradients. The solid line is the corresponding sample mean profile.

where τ_x and τ_y are the horizontally averaged streamwise and spanwise turbulent shear stresses. The vertical derivative of (3.4a,b) is

$$\frac{d^2}{d\xi^2} \left(\frac{\tau_x}{u_*^2} \right) = -\frac{h^2f}{u_*^2} \frac{dV}{dz}, \quad \frac{d^2}{d\xi^2} \left(\frac{\tau_y}{u_*^2} \right) = \frac{h^2f}{u_*^2} \frac{dU}{dz}, \quad (3.5a,b)$$

where $\xi = z/h$ is the normalized coordinate. Since the total turbulent shear stresses nearly collapse onto a single curve as a function of z/h , see (3.1) and figure 5, it is intuitive to conjecture that the wind gradients dU/dz and dV/dz normalized with $u_*^2/(h^2f)$ should also approximately collapse. To confirm this conjecture, figure 7 shows the streamwise and spanwise velocity gradients normalized by $u_*^2/(h^2f)$. Both tend to collapse to a single curve and are $O(1)$ above the surface layer. This indicates that $u_*^2/(h^2f)$ is indeed the appropriate scaling for the wind gradients above the surface layer (Lin & Segel 1988). Additionally, neither dU/dz nor dV/dz shows a uniform region, i.e. a region independent of z . This indicates that a z -less stratification layer is absent in NSBLs in the studied parameter range of μ and Ro .

To quantify the effectiveness of the scaling $u_*^2/(h^2f)$, figure 8 shows the mean absolute error (MAE) of the wind gradient profiles in figure 7. Here, the MAE is calculated as

$$\text{MAE}(X) = \frac{1}{n} \sum_{i=1}^n |X_i - \bar{X}|, \quad (3.6)$$

where $X = (h^2f/u_*^2)(dU/dz)$ and $(h^2f/u_*^2)(dV/dz)$, \bar{X} is the sample mean (i.e. the average of all cases) profile of X (see figure 7), i is the case number and $n = 20$ is the total number of all simulated cases (see table 1). Figure 8 shows clearly that the MAEs of wind gradients normalized by the scaling $u_*^2/(h^2f)$ are $O(0.1)$ above the surface layer. This quantitatively confirms the effective collapse of the wind gradients by the scaling $u_*^2/(h^2f)$ in the studied parameter range.

We remark that Zilitinkevich & Esau (2005) assumed that the wind gradients dU/dz and dV/dz above the surface layer scale as u_*/L_s and h^2f/L_s^2 , respectively. For NSBLs with large values of μ , we have shown that the boundary-layer height h scales as $\sqrt{L_f L_s}$, see (3.3) and figure 6. Under this condition, the scalings u_*/L_s , h^2f/L_s^2 and $u_*^2/(h^2f)$ are

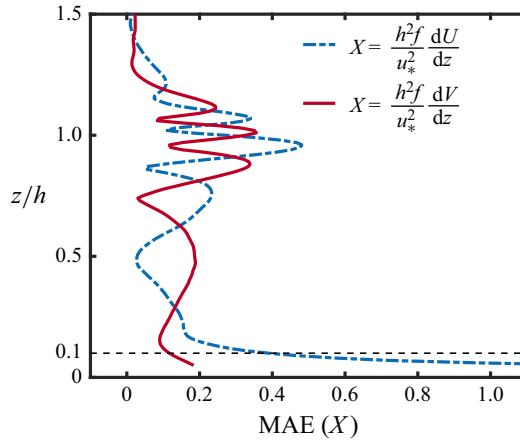


Figure 8. The MAE of (3.6) of the normalized wind gradients. The dashed line denotes the mean location of the surface-layer top.

equivalent since

$$\frac{u_*/L_s}{u_*^2/(h^2f)} = \frac{h^2}{L_f L_s} = c_s^2, \quad \frac{h^2 f/L_s^2}{u_*^2/(h^2f)} = \frac{h^4}{L_f^2 L_s^2} = c_s^4. \quad (3.7a,b)$$

However, choosing the scaling $u_*^2/(h^2f)$ may still be more convenient in practice, as it is directly derived from the vertical derivatives of the Ekman equations (3.5a,b) and hence ensures the normalized wind gradients above the surface layer are $O(1)$. In addition, for smaller values of μ , the difference between these scalings may exist since the boundary-layer height h ceases to scale as $\sqrt{L_f L_s}$ but scales as L_f .

4. Theoretical model

In this section, we will derive the analytical expressions of the GDL coefficients A and B for NSBLs under quasi-steady, barotropic and horizontally homogeneous conditions.

4.1. Analytical expression of A

We first determine the analytical expression of the GDL coefficient A . In the surface layer, of which the height is typically approximately 10% of the boundary-layer height h (Basu & Lacser 2017), the mean streamwise velocity U is assumed to be described by the MOST (Monin & Obukhov 1954; Businger *et al.* 1971)

$$\frac{\kappa U}{u_*} = \ln\left(\frac{z}{z_0}\right) + c_\psi \frac{z}{L_s}, \quad (4.1)$$

where c_ψ is an empirical constant and, according to (2.6a–c), $c_\psi = 4.8\kappa$ in this study. Note that (4.1) is also the basis of the wall model employed in the current LES.

The global properties of nocturnal stable ABLs

Above the surface layer or in the Ekman layer, [figure 7\(a\)](#) shows that the streamwise velocity gradient dU/dz scales as $u_*^2/(h^2f)$. Thus, we can assume

$$\kappa \frac{dU}{dz} = \frac{u_*^2}{h^2 f} f_u(\xi), \quad \xi = \frac{z}{h}, \quad (4.2)$$

where f_u is independent of Ro and μ . Integrating [\(4.2\)](#) from below to the top of the boundary layer and noting that $L_f = u_*/f$, we find

$$\frac{\kappa}{u_*} (U_g - U) = \frac{L_f}{h} \int_{\xi}^1 f_u(\xi') d\xi'. \quad (4.3)$$

We further assume the mean streamwise velocity U given by [\(4.1\)](#) and [\(4.3\)](#) matches at the interface $\xi = L_s/(c_1 h)$ or $z = L_s/c_1$, where c_1 is an empirical constant. Thus, by substituting [\(4.1\)](#) into [\(4.3\)](#), we find

$$\frac{\kappa U_g}{u_*} = \ln \left(\frac{L_s}{c_1 z_0} \right) + \frac{c_\psi}{c_1} + \frac{L_f}{h} \int_{L_s/c_1 h}^1 f_u(\xi') d\xi'. \quad (4.4)$$

Finally, substituting [\(1.1a\)](#) and [\(3.3\)](#) into [\(4.4\)](#) and noting that $\mu = L_f/L_s$, we obtain

$$A = \ln \mu - a_1 \sqrt{\mu} + a_2, \quad (4.5)$$

where

$$a_1 = \frac{1}{c_s} \int_{1/c_1 c_s \sqrt{\mu}}^1 f_u(\xi') d\xi', \quad a_2 = \ln c_1 - \frac{c_\psi}{c_1}. \quad (4.6)$$

Without knowing the form of f_u , the analytical expression of a_1 and thus of A cannot be obtained. However, [figures 6, 7\(a\)](#) and [9](#) indicate that $c_s = O(1)$, $c_1 = O(1)$ and $f_u = O(1)$ above the surface layer. Thus, $da_1/d\mu = f_u/(2c_1 c_s^2 \mu^{3/2}) = O(\mu^{-3/2}) = O(10^{-3})$ when $\mu = O(10^2)$, indicating that a_1 depends only very weakly on μ and hence can be assumed as a constant for simplicity. In this sense, the analytical expression of A is given by [\(4.5\)](#), which involves only two empirical constants (a_1, c_1) or equivalently (a_1, a_2). Note that [\(4.5\)](#) has the same structure as equation (24) of Zilitinkevich & Esau (2005). However, in our derivation we divide the boundary layer only into the surface layer and the Ekman layer, and requiring a z -less stratification layer is unnecessary. This makes the physics underlying the GDL more clear: it is a direct result of the asymptotic matching of the velocity profile between the surface layer and the Ekman layer. In addition, by making a comparison between [\(1.2a\)](#) and [\(4.5\)](#), we see the term $\ln(a_0 + m_A)$ in [\(1.2a\)](#) should be $a_0 + \ln m_A$. In this way, [\(1.2a\)](#) in the limit $\mu \gg 10$ approaches $A = \ln \mu - ac_s \sqrt{\mu} + a_0$, which is the same as [\(4.5\)](#) if $ac_s = a_1$ and $a_0 = a_2$.

4.2. Analytical expression of B

To determine the analytical expression of B , we recall that

$$\frac{d\tau_y}{dz} = f(U - U_g), \quad (4.7)$$

where τ_y is the spanwise component of the total shear stress tensor. We focus on the surface layer. Then, by substituting [\(1.1a\)](#) and [\(4.1\)](#) into [\(4.7\)](#) we obtain

$$\frac{\kappa}{f u_*} \frac{d\tau_y}{dz} = A + \ln \left(\frac{z}{L_f} \right) + c_\psi \frac{z}{L_s}. \quad (4.8)$$

The bottom boundary condition of (4.8) is $\tau_y(0) = 0$. Integrating (4.8) from 0 to z , one obtains

$$\frac{\kappa \tau_y}{f u_*} = (A - 1)z + z \ln \left(\frac{z}{L_f} \right) + c_\psi \frac{z^2}{2L_s}. \quad (4.9)$$

In the surface layer the eddy viscosity approach is assumed to be valid, such that (Zilitinkevich & Esau 2005)

$$\tau_y = K_m \frac{dV}{dz}, \quad K_m = \kappa u_* l, \quad \frac{1}{l} = \frac{1}{z} + \frac{c_\psi}{L_s}, \quad (4.10)$$

where V is the mean spanwise velocity. We remark that there is an extensive discussion in the literature about the eddy viscosity approach used here (see, e.g. Constantin & Johnson 2019), where the eddy viscosity K_m can be a function of height (Grisogono 1995), stability (Nieuwstadt 1983) and baroclinicity (Berger & Grisogono 1998). In these studies, the velocity profiles were derived based on assumed K_m profiles. However, correct K_m profiles in the whole boundary layer are very difficult to obtain and sometimes the eddy viscosity approach itself might become invalid in some regions of the boundary layer (Liu & Stevens 2022; Liu *et al.* 2023). Because the eddy viscosity approach is generally valid in the surface layer, it is adopted here. In particular, in the surface layer K_m in (4.10) is determined from (4.1) and the approximation $K_m dU/dz \approx u_*^2$.

By combining (4.9) and (4.10), we find

$$\frac{\kappa^2 dV}{f dz} = \left[A - 1 + \ln \left(\frac{z}{L_f} \right) \right] + c_\psi \frac{z}{L_s} \left[\left(A - \frac{1}{2} \right) + \ln \left(\frac{z}{L_f} \right) + \frac{c_\psi z}{2 L_s} \right]. \quad (4.11)$$

The bottom boundary condition of (4.11) is $V(0) = 0$. By integrating (4.11) from 0 to z one can determine the mean spanwise velocity V in the surface layer as

$$\frac{\kappa^2 V}{f} = z \left\{ \left[A - 2 + \ln \left(\frac{z}{L_f} \right) \right] + \frac{c_\psi z}{2 L_s} \left[A - 1 + \ln \left(\frac{z}{L_f} \right) + \frac{c_\psi z}{3 L_s} \right] \right\}. \quad (4.12)$$

Above the surface layer, figure 7(b) shows that the spanwise velocity gradient dV/dz scales as $u_*^2/(h^2 f)$ for NSBLs in the studied parameter range of Ro and μ . Thus, similar to the derivation of A , we can assume

$$\kappa \frac{dV}{dz} = -\frac{u_*^2}{h^2 f} f_v(\xi), \quad (4.13)$$

where f_v is independent of Ro and μ . Integrating (4.13) from below to the top of the boundary layer and noting that $L_f = u_*/f$, we obtain

$$\frac{\kappa}{u_*} (V_g - V) = -\frac{L_f}{h} \int_\xi^1 f_v(\xi') d\xi'. \quad (4.14)$$

We further assume the mean spanwise velocity V given by (4.12) and (4.14) matches at the interface $\xi = L_s/(c_2 h)$ or $z = L_s/c_2$, where c_2 is an empirical constant. Thus, by

substituting (4.12) into (4.14) and noting that $\mu = L_f/L_s$, we obtain

$$\frac{\kappa V_g}{u_*} = -\frac{L_f}{h} \int_{L_s/c_2h}^1 f_v d\xi' + \frac{1}{\kappa c_2\mu} [A - 2 - \ln(c_2\mu)] + \frac{1}{\kappa c_2\mu} \frac{c_\psi}{2c_2} \left[A - 1 - \ln(c_2\mu) + \frac{c_\psi}{3c_2} \right]. \quad (4.15)$$

Substituting (1.1b), (3.3) and (4.5) into (4.15), we find

$$B = b_1\sqrt{\mu} + \frac{b_2}{\sqrt{\mu}} + \frac{b_3}{\mu}, \quad (4.16)$$

where

$$\left. \begin{aligned} b_1 &= \frac{1}{c_s} \int_{1/c_2c_s\sqrt{\mu}}^1 f_v(\xi') d\xi', & b_2 &= \frac{a_1}{\kappa c_2} \left(1 + \frac{c_\psi}{2c_2} \right), \\ b_3 &= \frac{1}{\kappa c_2} \left[(1 + \ln c_2 - a_2) \left(1 + \frac{c_\psi}{2c_2} \right) + 1 - \frac{c_\psi^2}{6c_2^2} \right]. \end{aligned} \right\} \quad (4.17)$$

Finally, since the final term on the right-hand side of (4.16) is much smaller than the other two terms for $\mu \gg 10$, (4.16) can be written as

$$B = b_1\sqrt{\mu} + \frac{b_2}{\sqrt{\mu}}. \quad (4.18)$$

Similar to a_1 we can assume b_1 to be constant. Therefore, the analytical expression of B is given by (4.16), which also involves two empirical constants (b_1, c_2) since (a_1, c_1) are already given by (4.5). Note that (4.18) is different from equation (37) of Zilitinkevich & Esau (2005). The reason is as follows: in their derivation Zilitinkevich & Esau (2005) divided the surface layer into a logarithmic layer and a z -less stratification layer, and determined the spanwise velocity in the z -less stratification layer by only keeping the term proportional to z^2 . This leads to a discontinuity of the spanwise velocity across the interface of the logarithmic layer and the z -less stratification layer. As a result, their obtained equation (37) only included a single term similar to $b_1\sqrt{\mu}$, which underestimates the values of B for small and moderate μ and thus a correction constant b_0 is introduced to their general expression of B in (1.2b). Actually, (1.2b) reduces to $B = bc_s^3\sqrt{\mu} + b_0c_s/\sqrt{\mu}$ in the limit $\mu \gg 10$, which is the same as (4.18) when $bc_s^3 = b_1$ and $b_0c_s = b_2$. Because we treat the surface layer as a whole, the continuity of the spanwise velocity is satisfied automatically. As a result, our derivation gives a higher-order term, and hence, there is no need to introduce an additional correction constant. The effectiveness of this treatment also reveals the essential physics of the GDL more clearly.

4.3. Further remarks

We remark that when deriving the analytical expressions of A and B , i.e. (4.5) and (4.16) we have made two ansatzes: first, the streamwise and spanwise velocity profile between the inner and outer layers matches at a dimensionless height $1/(c_1c_s\sqrt{\mu})$ and $1/(c_2c_s\sqrt{\mu})$, respectively; and second, a_1 and b_1 can be approximated as constants that are independent of μ . These ansatzes enable us to predict well (A, B) without knowing the forms of (f_u, f_v) and with reasonable values of (c_1, c_2), see § 5 below. This fact also verifies the ansatzes themselves. However, if one assumes that the streamwise and spanwise velocity profiles

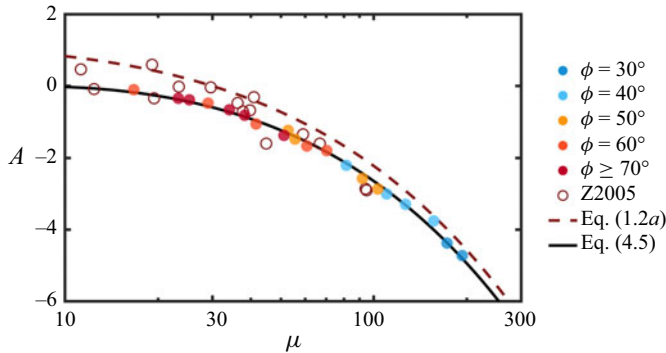


Figure 9. The GDL coefficient A vs the Kazanski–Monin parameter μ . Filled circles: simulation data of table 1; open circles: simulation data of Zilitinkevich & Esau (2005); dashed line: prediction of (1.2a) proposed by Zilitinkevich & Esau (2005); solid line: prediction of (4.5) with $a_1 = 0.72$, $c_1 = 2.25$ obtained by a least-squares fitting procedure.

between the inner and outer layers match at dimensionless heights independent of μ , then one would find these heights are too close to the top of boundary layer, and therefore, this assumption should be abandoned. On the other hand, if one assumes that a_1 and b_1 can be expanded in power series of $1/\sqrt{\mu}$, then the values of (c_1, c_2) cannot be determined without knowing the forms of (f_u, f_v) and thus this assumption should also be discarded. We further remark that the two velocities U_g and V_g can be obtained by substituting (4.5) and (4.16) into (1.1a,b). At first sight, these two velocities seem to be expressed to different orders of μ . However, we emphasize that the high-order term in B or V_g is obtained directly by ensuring the continuity of the spanwise velocity at the matching height, which differs from the formal asymptotic expansion. We also emphasize that, since (4.5) and (4.16) predict (A, B) accurately, they also predict well (U_g, V_g) and hence the geostrophic drag coefficient and the cross-isobaric angle.

5. Results and discussion

5.1. The performance of the analytical expressions of A and B

Figure 9 compares the GDL coefficient A as obtained from the theoretical predictions and simulation results of the present study with those of Zilitinkevich & Esau (2005). The results indicate that A decreases monotonically with increasing μ . The present simulation data (filled circles) collapse well onto a single curve and have much less scatter than the Zilitinkevich & Esau (2005) data. We remark that the simulation data of Zilitinkevich & Esau (2005) were averaged over the period $ft \in [1.3\pi, 2.1\pi]$. Because the flow above the boundary layer is neutrally stratified, the boundary layer is still developing during this period (figure 2). Thus, the simulation duration and time-averaging period should be the main reasons for their large scatter, although various other aspects such as the grid resolution, SGS model and numerical scheme may also have made some contributions. Even though their simulation data (open circles) display significant scatter, the overall trend agrees with ours (filled circles). These observations confirm the validity of the GDL for NSBLs described by (1.1a) within LES, extending its applicability across a wider range of μ .

In figure 9, the theoretical predictions are obtained by (1.2a) with the empirical constants $(a, a_0, c_{fa}, c_r, c_s) = (1.4, 1.65, 1, 0.6, 0.51)$ proposed by Zilitinkevich & Esau (2005) (dashed line), and (4.5) with $(a_1, c_1) = (0.72, 2.25)$ determined from the present

The global properties of nocturnal stable ABLs

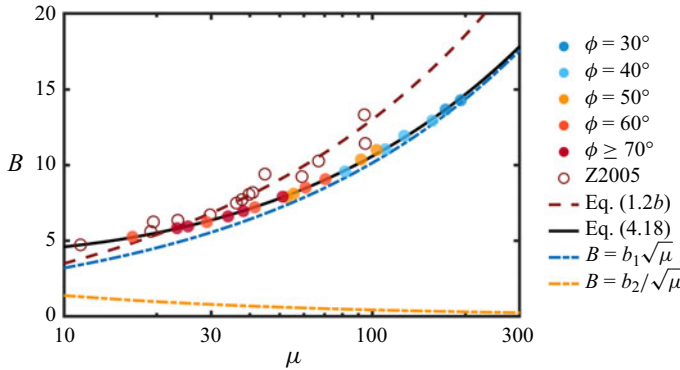


Figure 10. The GDL coefficient B vs the Kazanski–Monin parameter μ . Filled circles: simulation data of table 1; open circles: simulation data of Zilitinkevich & Esau (2005); dashed line: prediction of (1.2b) proposed by Zilitinkevich & Esau (2005); solid line: prediction of (4.18) with $b_1 = 1.02$, $c_2 = 0.86$ obtained by a least-squares fitting procedure; dashed-dotted lines: prediction of each term in (4.18).

LES database using a least-squares fitting procedure (solid line). The theoretical prediction of Zilitinkevich & Esau (2005) somewhat overestimates A , especially for small μ , and approaches asymptotically to the theoretical prediction of the present study for very large μ . The latter fact is consistent with our analysis given at the end of § 4.1, where we conclude that these two parameterizations are equivalent in the limit $\mu \gg 10$ if $ac_s = a_1$. Here, $a = 1.4$ and $c_s = 0.51$, and thus $ac_s = 0.71 \approx a_1 = 0.72$. The prediction of (4.5) agrees well with both the simulation data of the present study and those of Zilitinkevich & Esau (2005). This validates the present parameterization of A given by (4.5) with only two empirical constants (a_1, c_1) in the studied parameter range of μ and Ro . We remark that the surface-layer height normalized by the boundary-layer height can be approximated as $L_s/(c_1 h) = 1/(c_1 c_s \sqrt{\mu})$, which decreases as μ increases. In particular, it varies within the range of 5%–17% in the present simulations since $c_1 = 2.25$ (figure 9), $c_s = 0.62$ (figure 6) and $\mu \in [17, 193]$ (table 1). In addition, we remark that the empirical constants (a, a_0, c_{fa}, c_r, c_s) = (1.4, 1.65, 1, 0.6, 0.51) proposed by Zilitinkevich & Esau (2005) were optimized using their LES data. If optimized using our LES data, the prediction of (1.2a) matches well with our LES results (data not shown). This agreement is expected, as (1.2a) has five adjustable constants. In contrast, (4.5) has only two adjustable parameters and the main physics is clearer. The comparison of these two expressions thus indicates that high-fidelity data are necessary to obtain accurate parameterization of GDL coefficients.

Figure 10 compares the GDL coefficient B obtained from theoretical predictions and simulation results of the present study and of Zilitinkevich & Esau (2005). The simulation results indicate that B increases monotonically as μ increases. The present simulation data collapse well to a single curve, and hence validate the GDL for NSBLs over a wider range of μ . For small $\mu \lesssim 40$, the simulation data of Zilitinkevich & Esau (2005) agree well with our simulation results. For $\mu \gtrsim 40$ there is relatively large scatter in their data and B is significantly larger than in the present study (figure 10). As mentioned in § 2.3, the simulations conducted by Zilitinkevich & Esau (2005) were limited to $ft = 2.1\pi$, which does not allow for reliable determination of the friction velocity u_* and the cross-isobaric angle α_0 . Given that $B = (\kappa G/u_*) \sin \alpha_0$ is sensitive to changes in u_* and α_0 , this limitation likely contributed to their overestimation of B .

In figure 10, the theoretical predictions are obtained by (1.2b) with the empirical constants (b, b_0, c_{fb}, c_r, c_s) = (10, -2, 1, 0.6, 0.51) proposed by Zilitinkevich & Esau

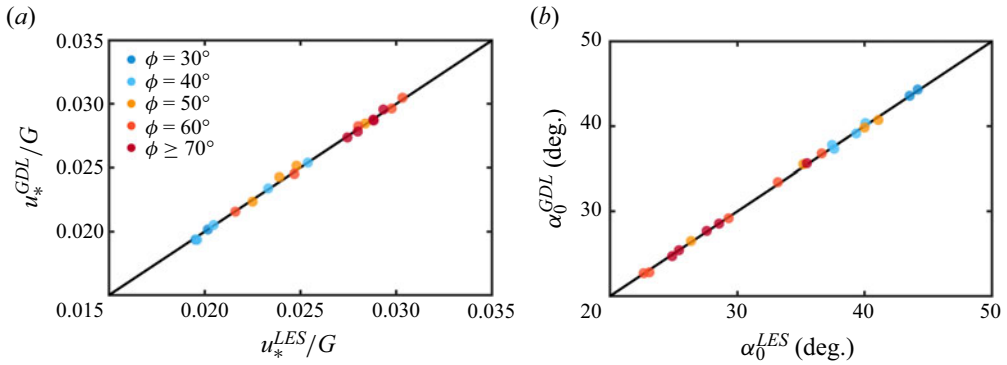


Figure 11. The comparison of (a) the geostrophic drag coefficient u_*/G and (b) the cross-isobaric angle $\alpha_0 = \arctan |V_g/U_g|$ obtained from the simulation data of table 1 and the GDL of (1.1a,b), where the coefficients A and B are parameterized by (4.5) and (4.18).

(2005) (dashed line), and (4.18) with $(b_1, c_2) = (1.02, 0.86)$ determined from the present LES database using a least-squares fitting procedure (solid line). The theoretical prediction of Zilitinkevich & Esau (2005) underestimates B for small μ and overestimates B for large μ . The latter fact is consistent with our analysis given at the end of § 4.2, where we conclude that these two parameterizations are equivalent in the limit $\mu \gg 10$ if $bc_s^3 = b_1$. Here, $b = 10$ and $c_s = 0.51$, and thus $bc_s^3 = 1.33 > b_1 = 1.02$, indicating that the prediction of (1.2b) becomes larger than that of (4.18) at large μ . The present prediction of (4.18) agrees well with all the simulation data of the present study. This validates the present parameterization of B given by (4.18) with only two empirical constants (b_1, c_2) in the studied parameter ranges of μ and Ro . In addition, figure 10 shows that the term $b_1\sqrt{\mu}$ approximates B well for large values of μ (blue dashed-dotted line). However, there are deviations between $b_1\sqrt{\mu}$ (blue dashed-dotted line) and B (solid line) for lower values of μ . The purpose of the term $b_2/\sqrt{\mu}$ (yellow dashed-dotted line) is to model these differences for lower μ .

5.2. The geostrophic drag coefficient and cross-isobaric angle

Figure 11 compares the geostrophic drag coefficient u_*/G and the cross-isobaric angle $\alpha_0 = \arctan(|V_g/U_g|)$ obtained from the present simulations with the GDL given by (1.1a,b), where the GDL coefficients A and B are parameterized by (4.5) and (4.18) using the empirical constants $(a_1, b_1, c_1, c_2) = (0.72, 1.02, 2.25, 0.86)$ determined in § 5.1. The figure shows that the agreement between the new parametrizations and all the numerical data is good. Figure 11(a) shows that our simulations cover the range $0.0195 \leq u_*/G \leq 0.0304$, which covers the typical range observed in atmospheric measurements. Figure 11(b) shows that the cross-isobaric angle varies between 23° and 44° and that all LES data collapse to the theoretical curve. This good agreement is expected as $\alpha_0 = \arcsin[(Bu_*)/(\kappa G)]$ and B (figure 9b) and u_*/G (figure 11a) have already been predicted accurately. Note that the cross-isobaric angle α_0 in NSBLs (see table 1 and figure 11b) is usually larger than that in conventionally neutral (Liu *et al.* 2021a) and convective ABLs (Liu *et al.* 2023). This is a typical phenomenon in ABLs: the wind veer is stronger in stable conditions than in neutral and convective conditions.

The geostrophic drag coefficient u_*/G and the cross-isobaric angle α_0 are two key global properties of ABLs, which are fundamental for constructing wind profiles throughout the entire turbulent boundary layer. Therefore, we present the geostrophic drag coefficient

The global properties of nocturnal stable ABLs

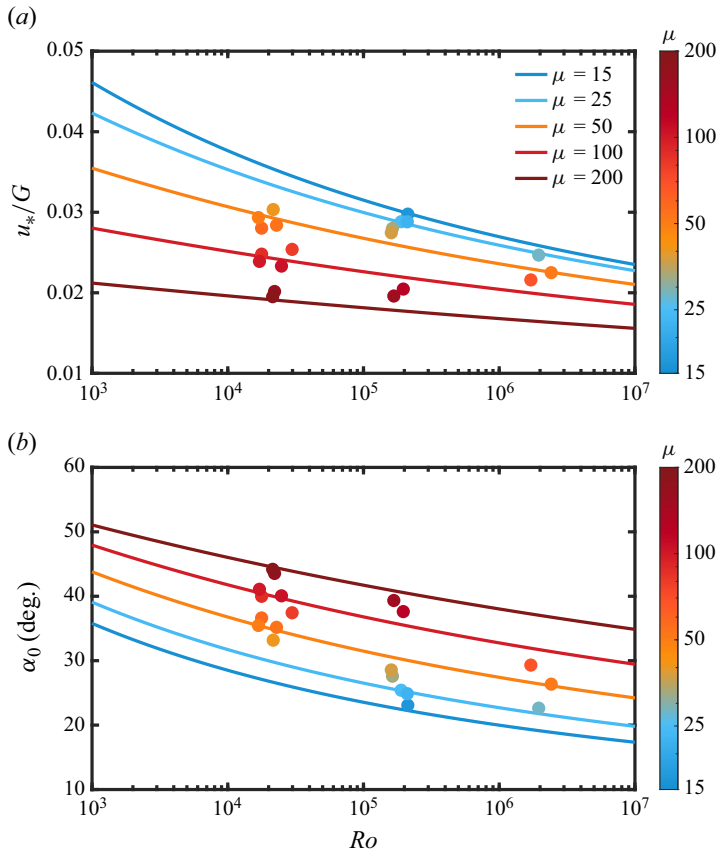


Figure 12. The (a) geostrophic drag coefficient u_*/G and (b) cross-isobaric angle α_0 obtained from the simulation data of table 1 (filled circles) and the GDL of (1.1a,b) (solid lines), where the coefficients A and B are parameterized by (4.5) and (4.18).

u_*/G and the cross-isobaric angle $\alpha_0 = \arctan(|V_g/U_g|)$ in figure 12. The simulation results (filled circles) are in good agreement with the GDL results (solid lines), see also figure 11. The figure demonstrates that u_*/G decreases with increasing Ro or μ . Notably, u_*/G exhibits a strong dependence on Ro for low μ (e.g. $\mu = 15$) and becomes nearly independent of Ro for high μ (e.g. $\mu = 200$). Furthermore, figure 12(b) illustrates that α_0 decreases with increasing Ro , and increases with increasing μ . The dependence of α_0 on Ro is more pronounced for lower μ .

6. Conclusions

We investigate numerically and theoretically the global properties of NSBLs under quasi-steady, barotropic and horizontally homogeneous conditions. In particular, we focus on NSBLs with the Kazanski–Monin parameter $\mu = O(10) \sim O(10^2)$ since they are considered neutral when $|\mu| \ll 10$ and may be intermittent when $\mu \gg 10^2$. To get high-fidelity data for NSBLs, we perform a series of carefully designed LESs with sufficiently high grid resolutions and for long time durations. These simulations cover a wider range of the Kazanski–Monin parameter $\mu \in [16.7, 193.3]$ and the Rossby number $Ro \in [1.68 \times 10^4, 2.42 \times 10^6]$ than previously considered. We find that the

boundary-layer height h scales as $\sqrt{L_f L_s}$, and both the streamwise and spanwise wind gradients scale as $u_*^2/(h^2 f)$, where L_f is the Ekman length scale, L_s is the surface Obukhov length, u_* is the friction velocity and f is the Coriolis parameter.

We study the GDL for NSBLs to obtain an analytical prediction for the global properties like the geostrophic drag coefficient u_*/G and the cross-isobaric angle α_0 as a function of the Kazanski–Monin parameter μ and the Rossby number Ro . We first show that the GDL coefficients A and B obtained from carefully performed LES collapse to single curves as functions of μ . This verifies the GDL for NSBLs over an extended range of μ within LES. We emphasize that the present LES employs the wall model based on the MOST (Monin & Obukhov 1954). Thus, the concept of ‘grid convergence’ does not strictly apply here. For example, the magnitude of total shear stress and potential temperature flux at the surface decrease as the grid resolution increases. This grid-sensitivity issue should be kept in mind when one compares the LES results with direct numerical simulations and experimental measurements. In addition, because the MOST is not valid for very stable boundary layers with $\mu \gg O(10^2)$, the current LES is unable to simulate these cases. Therefore, to verify the GDL for NSBLs over the whole range of μ using high-fidelity LES data, one may need to utilize a partially wall-resolved LES (Chinita, Matheou & Miranda 2022).

We derived new analytical expressions of A and B by using three crucial insights: (i) the boundary-layer height can be parameterized by the approach of Zilitinkevich (1972), (ii) the wind gradients can be scaled by $u_*^2/(h^2 f)$ and (iii) the streamwise and spanwise velocities are continuous in the boundary layer. In addition, we assume that the eddy viscosity approach is valid in the surface layer and the mean streamwise velocity therein can be predicted by the MOST (Monin & Obukhov 1954). This allows a direct derivation, without the need to assume z -less stratification, of analytical expressions for A (4.5) and B (4.18) with just four empirical constants. These constants can be determined from measurements or simulations, and here we use the latter. The good agreement between the theoretical predictions and the simulation results confirms the validity of the new analytical expressions of A and B for the studied range of μ and Ro .

The drag law exists in various wall-bounded turbulent flows, which may have different formulations in different flows. For example, it manifests as the friction law in channel and pipe flows (Pope 2000), the convective logarithmic friction law in convective boundary layers (Tong & Ding 2020; Liu *et al.* 2023) and the GDL in neutral and stable boundary layers (Zilitinkevich & Esau 2005; Liu *et al.* 2021a). Physically, the existence of drag law is a direct result of the asymptotic matching of the velocity profiles between the inner and outer layers (Zilitinkevich 1975). From this perspective, our results not only advance our physical understanding of the GDL for NSBLs, but also can be very helpful for deepening our understanding of wall turbulence in general (Smits *et al.* 2011; Chung *et al.* 2021).

Funding. This work was supported by the National Natural Science Foundation of China (grant no. 12388101), the National Natural Science Fund for Excellent Young Scientists Fund Program (Overseas) and the Supercomputing Center of the University of Science and Technology of China. This project has received funding from the European Research Council under the Horizon Europe program (grant no. 101124815).

Declaration of interests. The authors report no conflict of interest.

Author ORCIDs.

🔗 Luoqin Liu <https://orcid.org/0000-0002-6020-3702>;

🔗 Xiyun Lu <https://orcid.org/0000-0002-0737-6460>;

🔗 Richard J.A.M. Stevens <https://orcid.org/0000-0001-6976-5704>.

The global properties of nocturnal stable ABLs

REFERENCES

- ABKAR, M. & MOIN, P. 2017 Large eddy simulation of thermally stratified atmospheric boundary layer flow using a minimum dissipation model. *Boundary-Layer Meteorol.* **165** (3), 405–419.
- ALBERTSON, J.D. 1996 Large eddy simulation of land-atmosphere interaction. PhD thesis, University of California.
- ALBERTSON, J.D. & PARLANGE, M.B. 1999 Surface length-scales and shear stress: implications for land-atmosphere interaction over complex terrain. *Water Resour. Res.* **35**, 2121–2132.
- ARYA, S.P.S. 1975 Geostrophic drag and heat transfer relations for the atmospheric boundary layer. *Q. J. R. Meteorol. Soc.* **101**, 147–161.
- ARYA, S.P.S. 1978 Comparative effects of stability, baroclinity and the scale-height ratio on drag laws for the atmospheric boundary layer. *J. Atmos. Sci.* **35** (1), 40–46.
- ARYA, S.P.S. & WYNGAARD, J.C. 1975 Effect of baroclinicity on wind profiles and the geostrophic drag law for the convective planetary boundary layer. *J. Atmos. Sci.* **32**, 767–778.
- BASU, S. & HOLTSLAG, A.A.M. 2023 A novel approach for deriving the stable boundary layer height and eddy viscosity profiles from the Ekman equations. *Boundary-Layer Meteorol.* **187**, 105–115.
- BASU, S. & LACSER, A. 2017 A cautionary note on the use of Monin–Obukhov similarity theory in very high-resolution large-eddy simulations. *Boundary-Layer Meteorol.* **163** (2), 351–355.
- BEARE, R.J., *et al.* 2006 An intercomparison of large eddy simulations of the stable boundary layer. *Boundary-Layer Meteorol.* **118**, 247–272.
- BERGER, B.W. & GRISOGONO, B. 1998 The baroclinic, variable eddy viscosity Ekman layer. *Boundary-Layer Meteorol.* **87**, 363–380.
- BLACKADAR, A.K. & TENNEKES, H. 1968 Asymptotic similarity in neutral barotropic planetary boundary layers. *J. Atmos. Sci.* **25** (6), 1015–1020.
- BUSINGER, J.A., WYNGAARD, J.C., IZUMI, Y. & BRADLEY, E.F. 1971 Flux-profile relationships in the atmospheric surface layer. *J. Atmos. Sci.* **28** (2), 181–189.
- BYUN, D.W. 1991 Determination of similarity functions of the resistance laws for the planetary boundary layer using surface-layer similarity functions. *Boundary-Layer Meteorol.* **57** (1), 17–48.
- CAUGHEY, S.J., WYNGAARD, J.C. & KAIMAL, J.C. 1979 Turbulence in the evolving stable boundary layer. *J. Atmos. Sci.* **36**, 1041–1052.
- CHINITA, M.J., MATHEOU, G. & MIRANDA, P.M.A. 2022 Large-eddy simulation of very stable boundary layers. Part I. Modeling methodology. *Q. J. R. Meteorol. Soc.* **148**, 1805–1823.
- CHUNG, D., HUTCHINS, N., SCHULTZ, M.P. & FLACK, K.A. 2021 Predicting the drag of rough surfaces. *Annu. Rev. Fluid Mech.* **53**, 439–471.
- CONSTANTIN, A. & JOHNSON, R.S. 2019 Atmospheric Ekman flows with variable eddy viscosity. *Boundary-Layer Meteorol.* **170**, 395–414.
- COOKE, J., JEROLMACK, D. & PARK, G.I. 2024 Mesoscale structure of the atmospheric boundary layer across a natural roughness transition. *Proc. Natl Acad. Sci. USA* **121**, e2320216121.
- COUVREUX, F., *et al.* 2020 Intercomparison of large-eddy simulations of the antarctic boundary layer for very stable stratification. *Boundary-Layer Meteorol.* **176**, 369–400.
- DAI, Y., BASU, S., MARONGA, B. & DE ROODE, S.R. 2021 Addressing the grid-size sensitivity issue in large-eddy simulations of stable boundary layers. *Boundary-Layer Meteorol.* **178**, 63–89.
- DELAGE, Y. 1997 Parameterising sub-grid scale vertical transport in atmospheric models under statically stable conditions. *Boundary-Layer Meteorol.* **82**, 23–48.
- DERBYSHIRE, S.H. 1990 Nieuwstadt’s stable boundary layer revisited. *Q. J. R. Meteorol. Soc.* **116**, 127–158.
- VAN DOP, H. & AXELSEN, S. 2007 Large eddy simulation of the stable boundary-layer: a retrospect to Nieuwstadt’s early work. *Flow Turbul. Combust.* **79**, 235–249.
- DOUGHERTY, J.P. 1961 The anisotropy of turbulence at the meteor level. *J. Atmos. Terr. Phys.* **21** (2), 210–213.
- EKMAN, V.W. 1905 On the influence of the Earth’s rotation on ocean-currents. *Ark. Mat. Astron. Fys.* **2**, 1–52.
- ELLISON, T.H. 1955 The Ekman spiral. *Q. J. R. Meteorol. Soc.* **81** (350), 637–638.
- FERNANDO, H.J.S. & WEIL, J.C. 2010 Whither the stable boundary layer? *Bull. Am. Meteor. Soc.* **91**, 1475–1484.
- FLOORS, R., PEÑA, A. & GRYNING, S.-E. 2015 The effect of baroclinicity on the wind in the planetary boundary layer. *Q. J. R. Meteorol. Soc.* **141**, 619–630.
- GADDE, S.N., STIEREN, A. & STEVENS, R.J.A.M. 2021 Large-eddy simulations of stratified atmospheric boundary layers: comparison of different subgrid models. *Boundary-Layer Meteorol.* **178** (3), 363–382.
- GARRATT, J.R. 1983 Surface influence upon vertical profiles in the nocturnal boundary layer. *Boundary-Layer Meteorol.* **26** (1), 69–80.

- GRACHEV, A.A., ANDREAS, E.L., FAIRALL, C.W., GUEST, P.S. & PERSSON, P.O.G. 2013 The critical Richardson number and limits of applicability of local similarity theory in the stable boundary layer. *Boundary-Layer Meteorol.* **147**, 51–82.
- GRACHEV, A.A., FAIRALL, C.W., PERSSON, P.O.G., ANDREAS, E.L. & GUEST, P.S. 2005 Stable boundary-layer scaling regimes: the SHEBA data. *Boundary-Layer Meteorol.* **116**, 201–235.
- GRISOGONO, B. 1995 A generalized Ekman layer profile with gradually varying eddy diffusivities. *Q. J. R. Meteorol. Soc.* **121**, 445–453.
- GRYNING, S.-E., BATCHVAROVA, E., BRÜMMER, B., JØRGENSEN, H. & LARSEN, S. 2007 On the extension of the wind profile over homogeneous terrain beyond the surface boundary layer. *Boundary-Layer Meteorol.* **124** (2), 251–268.
- HESS, G.D. 2004 The neutral, barotropic planetary boundary layer, capped by a low-level inversion. *Boundary-Layer Meteorol.* **110** (3), 319–355.
- HUANG, J. & BOU-ZEID, E. 2013 Turbulence and vertical fluxes in the stable atmospheric boundary layer. Part I. A large-eddy simulation study. *J. Atmos. Sci.* **70**, 1513–1527.
- KADANTSEV, E., MORTIKOV, E. & ZILITINKEVICH, S. 2021 The resistance law for stably stratified atmospheric planetary boundary layers. *Q. J. R. Meteorol. Soc.* **147**, 2233–2243.
- KATUL, G.G., KONINGS, A.G. & PORPORATO, A. 2011 Mean velocity profile in a sheared and thermally stratified atmospheric boundary layer. *Phys. Rev. Lett.* **107** (26), 268502.
- KAZANSKI, A.B. & MONIN, A.S. 1961 On the dynamic interaction between the atmosphere and the Earth's surface. *Izv. Acad. Sci. USSR Geophys. Ser. Engl. Transl.* **5**, 514–515.
- KELLY, M. & GRYNING, S.-E. 2010 Long-term mean wind profiles based on similarity theory. *Boundary-Layer Meteorol.* **136**, 377–390.
- KIM, J. & LEONARD, A. 2024 The early days and rise of turbulence simulation. *Annu. Rev. Fluid Mech.* **56**, 21–44.
- KLEMP, J.B. & LILLY, D.K. 1978 Numerical simulation of hydrostatic mountain waves. *J. Atmos. Sci.* **68**, 46–50.
- KRISHNA, K. 1980 The planetary-boundary-layer model of Ellison (1956) – a retrospect. *Boundary-Layer Meteorol.* **19** (3), 293–301.
- LACSER, A. & ARYA, S.P.S. 1986 A numerical model study of the structure and similarity scaling of the nocturnal boundary layer (NBL). *Boundary-Layer Meteorol.* **35**, 369–385.
- LEMONE, M.A., *et al.* 2019 100 years of progress in boundary layer meteorology. *Meteorol. Monogr.* **59**, 9.1–9.85.
- LENSCHOW, D.H., LI, X.S., ZHU, C.J. & STANKOV, B.B. 1988 The stably stratified boundary layer over the great plains. I. Mean and turbulence structure. *Boundary-Layer Meteorol.* **42**, 95–121.
- LIN, C.C. & SEGEL, L.A. 1988 *Mathematics Applied to Deterministic Problems in the Natural Sciences*. Society for Industrial and Applied Mathematics.
- LIU, L., GADDE, S.N. & STEVENS, R.J.A.M. 2021a Geostrophic drag law for conventionally neutral atmospheric boundary layers revisited. *Q. J. R. Meteorol. Soc.* **147**, 847–857.
- LIU, L., GADDE, S.N. & STEVENS, R.J.A.M. 2021b Universal wind profile for conventionally neutral atmospheric boundary layers. *Phys. Rev. Lett.* **126**, 104502.
- LIU, L., GADDE, S.N. & STEVENS, R.J.A.M. 2023 The mean wind and potential temperature flux profiles in convective boundary layers. *J. Atmos. Sci.* **80** (8), 1893–1903.
- LIU, L., LU, X. & STEVENS, R.J.A.M. 2024 Geostrophic drag law in conventionally neutral atmospheric boundary layer: simplified parametrization and numerical validation. *Boundary-Layer Meteorol.* **190** (8), 37.
- LIU, L. & STEVENS, R.J.A.M. 2021 Effects of atmospheric stability on the performance of a wind turbine located behind a three-dimensional hill. *Renew. Energy* **175**, 926–935.
- LIU, L. & STEVENS, R.J.A.M. 2022 Vertical structure of conventionally neutral atmospheric boundary layers. *Proc. Natl Acad. Sci. USA* **119**, e2119369119.
- MAHRT, L. 2014 Stably stratified atmospheric boundary layers. *Annu. Rev. Fluid Mech.* **46**, 23–45.
- MARONGA, B., KNIGGE, C. & RAASCH, S. 2020 An improved surface boundary condition for large-eddy simulations based on Monin–Obukhov similarity theory: evaluation and consequences for grid convergence in neutral and stable conditions. *Boundary-Layer Meteorol.* **174**, 297–325.
- MARONGA, B. & LI, D. 2022 An investigation of the grid sensitivity in large-eddy simulations of the stable boundary layer. *Boundary-Layer Meteorol.* **182**, 251–273.
- MARUSIC, I. & MONTY, J.P. 2019 Attached eddy model of wall turbulence. *Annu. Rev. Fluid Mech.* **51** (1), 49–74.
- MARUSIC, I., MONTY, J.P., HULTMARK, M. & SMITS, A.J. 2013 On the logarithmic region in wall turbulence. *J. Fluid Mech.* **716**, R3.

The global properties of nocturnal stable ABLs

- MOENG, C.-H. 1984 A large-eddy simulation model for the study of planetary boundary-layer turbulence. *J. Atmos. Sci.* **41**, 2052–2062.
- MOMEN, M. & BOU-ZEID, E. 2017 Mean and turbulence dynamics in unsteady Ekman boundary layers. *J. Fluid Mech.* **816**, 209–242.
- MOMEN, M., BOU-ZEID, E., PARLANGE, M.B. & GIOMETTO, M. 2018 Modulation of mean wind and turbulence in the atmospheric boundary layer by baroclinicity. *J. Atmos. Sci.* **75**, 3797–3821.
- MONIN, A.S. & OBUKHOV, A.M. 1954 Basic laws of turbulent mixing in the surface layer of the atmosphere. *Tr. Akad. Nauk SSSR Geophys. Inst.* **24** (151), 163–187.
- NARASIMHAN, G., GAYME, D.F. & MENEVEAU, C. 2024 Analytical model coupling Ekman and surface layer structure in atmospheric boundary layer flows. *Boundary-Layer Meteorol.* **190**, 16.
- NIEUWSTADT, F.T.M. 1983 On the solution of the stationary, baroclinic Ekman-layer equations with a finite boundary-layer height. *Boundary-Layer Meteorol.* **26**, 377–390.
- NIEUWSTADT, F.T.M. 1984 The turbulent structure of the stable, nocturnal boundary layer. *J. Atmos. Sci.* **41** (14), 2202–2216.
- OBUKHOV, A.M. 1946 Turbulence in an atmosphere with inhomogeneous temperature. *Trans. Inst. Teoret. Geoz. Akad. Nauk SSSR* **1**, 95–115.
- OZMIDOV, R.V. 1965 On the turbulent exchange in a stably stratified ocean. *Izv. Acad. Sci. USSR Atmos. Ocean. Phys.* **1** (8), 853–860.
- POPE, S.B. 2000 *Turbulent Flows*. Cambridge University Press.
- RICCO, P. & SKOTE, M. 2022 Integral relations for the skin-friction coefficient of canonical flows. *J. Fluid Mech.* **943**, A50.
- ROSSBY, C.G. & MONTGOMERY, R.B. 1935 The layers of frictional influence in wind and ocean currents. *Pap. Phys. Oceanogr. Meteor.* **3** (3), 1–101.
- SALESKY, S.T., CHAMECKI, M. & BOU-ZEID, E. 2017 On the nature of the transition between roll and cellular organization in the convective boundary layer. *Boundary-Layer Meteorol.* **163**, 41–68.
- SCHMID, M.F., LAWRENCE, G.A., PARLANGE, M.B. & GIOMETTO, M.G. 2019 Volume averaging for urban canopies. *Boundary-Layer Meteorol.* **173** (3), 349–372.
- SCHULTZ, M.P., BENDICK, J.A., HOLM, E.R. & HERTEL, W.M. 2011 Economic impact of biofouling on a naval surface ship. *Biofouling* **27**, 87–98.
- SHAH, S.K. & BOU-ZEID, E. 2014 Direct numerical simulations of turbulent Ekman layers with increasing static stability: modifications to the bulk structure and second-order statistics. *J. Fluid Mech.* **760**, 494–539.
- SMITS, A.J. 2022 Batchelor prize lecture: measurements in wall-bounded turbulence. *J. Fluid Mech.* **940**, A1.
- SMITS, A.J., MCKEON, B.J. & MARUSIC, I. 2011 High Reynolds number wall turbulence. *Annu. Rev. Fluid Mech.* **43**, 353–375.
- SORBJAN, Z. 1986 On similarity in the atmospheric boundary layer. *Boundary-Layer Meteorol.* **34** (4), 377–397.
- SPALART, P.R. & MCLEAN, J.D. 2011 Drag reduction: enticing turbulence, and then an industry. *Phil. Trans. R. Soc. A* **369**, 1556–1569.
- STIPERSKI, I. & CALAF, M. 2018 Dependence of near-surface similarity scaling on the anisotropy of atmospheric turbulence. *Q. J. R. Meteorol. Soc.* **144**, 641–657.
- STOLL, R., GIBBS, J.A., SALESKY, S.T., ANDERSON, W. & CALAF, M. 2020 Large-eddy simulation of the atmospheric boundary layer. *Boundary-Layer Meteorol.* **177**, 541–581.
- STOLL, R. & PORTÉ-AGEL, F. 2008 Large-eddy simulation of the stable atmospheric boundary layer using dynamic models with different averaging schemes. *Boundary-Layer Meteorol.* **126**, 1–28.
- STULL, R.B. 1988 *An Introduction to Boundary Layer Meteorology*. Kluwer Academic.
- SULLIVAN, P.P., WEIL, J.C., PATTON, E.G., JONKER, H.J.J. & MIRONOV, D.V. 2016 Turbulent winds and temperature fronts in large-eddy simulations of the stable atmospheric boundary layer. *J. Atmos. Sci.* **73** (4), 1815–1840.
- TENNEKES, H. 1973 The logarithmic wind profile. *J. Atmos. Sci.* **30** (2), 234–238.
- TENNEKES, H. & LUMLEY, J.L. 1972 *A First Course in Turbulence*. MIT Press.
- TONG, C. & DING, M. 2020 Velocity-defect laws, log law and logarithmic friction law in the convective atmospheric boundary layer. *J. Fluid Mech.* **883**, A36.
- TOWNSEND, A.A. 1976 *Structure of Turbulent Shear Flow*, 2nd edn. Cambridge University Press.
- VAN DE WIEL, B.J.H., MOENE, A.F., STEENEVELD, G.J., BAAS, P., BOSVELD, F.C. & HOLTSLAG, A.A.M. 2010 A conceptual view on inertial oscillations and nocturnal low-level jets. *J. Atmos. Sci.* **67**, 2679–2689.
- VICKERS, D. & MAHRT, L. 2004 Evaluating formulations of stable boundary layer height. *J. Appl. Meteorol.* **43**, 1736–1749.

- VREMAN, B., GEURTS, B. & KUERTEN, H. 1994 On the formulation of the dynamic mixed subgrid-scale model. *Phys. Fluids* **6**, 4057–4059.
- WITTICH, K.P. 1991 The nocturnal boundary layer over Northern Germany: an observational study. *Boundary-Layer Meteorol.* **55**, 47–66.
- WYNGAARD, J.C. & COTÉ, O.R. 1972 Cospectral similarity in the atmospheric surface layer. *Q. J. R. Meteorol. Soc.* **98**, 590–603.
- YOKOYAMA, O., GAMO, M. & YAMAMOTO, S. 1979 The vertical profiles of the turbulence quantities in the atmospheric boundary layer. *J. Meteorol. Soc. Japan* **57**, 264–272.
- ZILITINKEVICH, S.S. 1969 On the computation of the basic parameters of the interaction between the atmosphere and the ocean. *Tellus* **21** (1), 17–24.
- ZILITINKEVICH, S.S. 1972 On the determination of the height of the Ekman boundary layer. *Boundary-Layer Meteorol.* **3**, 141–145.
- ZILITINKEVICH, S.S. 1975 Resistance laws and prediction equations for the depth of the planetary boundary layer. *J. Atmos. Sci.* **32** (4), 741–752.
- ZILITINKEVICH, S.S. 1989a The temperature profile and heat transfer law in a neutrally and stably stratified planetary boundary layer. *Boundary-Layer Meteorol.* **49**, 1–5.
- ZILITINKEVICH, S.S. 1989b Velocity profiles, the resistance law and the dissipation rate of mean flow kinetic energy in a neutrally and stably stratified planetary boundary layer. *Boundary-Layer Meteorol.* **46** (4), 367–387.
- ZILITINKEVICH, S.S. & DEARDORFF, J.W. 1974 Similarity theory for the planetary boundary layer of time-dependent height. *J. Atmos. Sci.* **31** (5), 1449–1452.
- ZILITINKEVICH, S.S. & ESAU, I.N. 2002 On integral measures of the neutral barotropic planetary boundary layer. *Boundary-Layer Meteorol.* **104** (3), 371–379.
- ZILITINKEVICH, S.S. & ESAU, I.N. 2005 Resistance and heat-transfer laws for stable and neutral planetary boundary layers: old theory advanced and re-evaluated. *Q. J. R. Meteorol. Soc.* **131** (609), 1863–1892.
- ZILITINKEVICH, S.S., ESAU, I. & BAKLANOV, A. 2007 Further comments on the equilibrium height of neutral and stable planetary boundary layers. *Q. J. R. Meteorol. Soc.* **133** (622), 265–271.
- ZILITINKEVICH, S., JOHANSSON, P.E., MIRONOV, D.V. & BAKLANOV, A. 1998 A similarity-theory model for wind profile and resistance law in stably stratified planetary boundary layers. *J. Wind Engng Ind. Aerodyn.* **74–76**, 209–218.